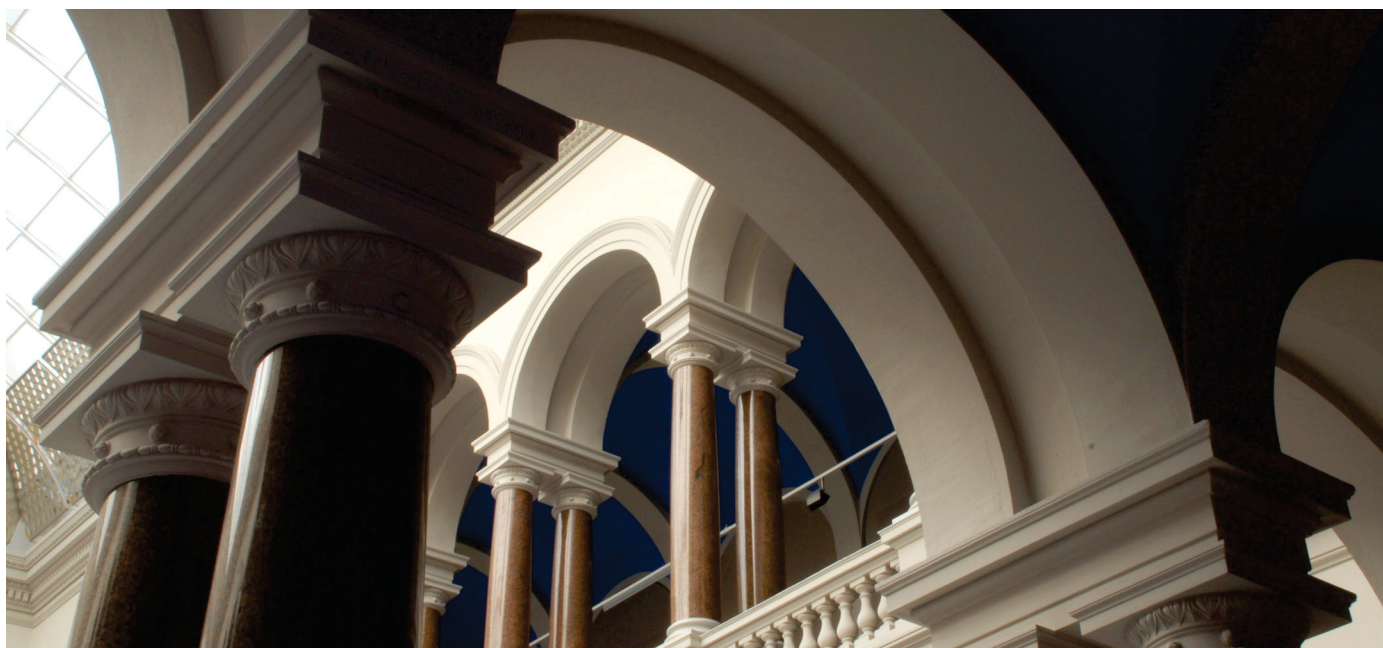


Henning Bonart, Christian Kahle, Jens-Uwe Repke

Optimal Control of Droplets on a Solid Surface Using Distributed Contact Angles

Journal article | Accepted manuscript (Postprint)

This version is available at <https://doi.org/10.14279/depositononce-10479>



Bonart, H., Kahle, C., & Repke, J.-U. (2020). Optimal Control of Droplets on a Solid Surface Using Distributed Contact Angles. *Langmuir*, 36(30), 8894–8903. <https://doi.org/10.1021/acs.langmuir.0c01242>

Terms of Use

Copyright applies. A non-exclusive, non-transferable and limited right to use is granted. This document is intended solely for personal, non-commercial use.

WISSEN IM ZENTRUM
UNIVERSITÄTSBIBLIOTHEK

Technische
Universität
Berlin

Optimal Control of Droplets on a Solid Surface using Distributed Contact Angles

Henning Bonart,^{*,†} Christian Kahle,[‡] and Jens-Uwe Repke[†]

[†]*Technische Universität Berlin, Process Dynamics and Operations Group, Straße des 17.*

Juni 135, 10623 Berlin, Germany

[‡]*Universität Koblenz-Landau, Universitätsstraße 1, 56070 Koblenz, Germany*

E-mail: henning.bonart@tu-berlin.de

Abstract

Controlling the shape and position of moving and pinned droplets on a solid surface is an important feature often found in microfluidic applications. However, automating them, e.g., for high-throughput applications, does rarely involve model-based optimal control strategies. In this work, we demonstrate the optimal control of both the shape and position of a droplet sliding on an inclined surface. This basic test case is a fundamental building block in plenty of microfluidic designs. The static contact angle between the solid surface, the surrounding gas, and the liquid droplet serves as the control variable. By using several control patches, e.g., like done in electrowetting, the contact angles are allowed to vary in space and time. In computer experiments, we are able to calculate mathematically optimal contact angle distributions using gradient-based optimization. The dynamics of the droplet are described by the Cahn–Hilliard–Navier–Stokes equations. We anticipate our demonstration to be the starting point for more sophisticated optimal design and control concepts.

Keywords

Droplets, optimal control, contact angle, phase field model, electrowetting, lab-on-a-chip

Introduction

In many droplet-based microfluidic processes and applications the precise shape and position of the droplets over time play a significant role for the performance of the device. One example is the transport of droplets in a lab-on-a-chip device. Here, the droplets get merged, split and mixed at specific positions on the chip¹. Thereby, the shape of the droplets influences the heat and mass that is exchanged with the solid surface and the surrounding fluid phase². To enforce desired droplet movements and shapes, surfaces with complex patterns of different wettability were heuristically designed³⁻⁸. In addition, active adjustment of droplets were performed^{1,9,10}.

A second example are optical applications where liquid droplets act as flexible lenses with continuous refraction power ranges¹¹⁻¹⁷. By adjusting their shape and position using active adjustment of the contact angles, the curvature and hence the focal length can be precisely tuned. This allows for interesting applications like a liquid lens in cameras¹⁸; see the recent review by Mishra et al. for details¹⁹.

To control the shape or position of droplets or curved interfaces, some works proposed feedback controllers²⁰⁻²³. While these controllers fulfill their task and allow for promising applications, they enable only a rather crude adjustment of the droplet's position and, in particular, the shape of the curved interface. Especially for applications in optofluidics however, precise control over the shape of the interface is crucial¹³.

A promising remedy is model-based optimal control. Mathematical optimal control strategies had, and continue to have, great impact in industries like aviation, automotive, and chemical, see the review by Lee on model predictive control²⁴. Yet only very few articles describe optimal control within the scope of droplet-based microfluidics. This includes the

control of the footprint and shape of a static droplet²⁵, the position of a moving droplet and its shape in absence of gravity²⁶, and the position of the gas-liquid interface of rising liquid in a capillary²⁷. However, the simultaneous and precise control of both the shape and position of a droplet to fulfill a target in a mathematically optimal way is absent.

Therefore, we present the surface based control of both the shape and position of droplets. The static contact angle between the solid surface, the surrounding gas and the liquid droplet serves as the control variable. The dynamics of the droplet and the gas-liquid interface are described by the Cahn–Hilliard–Navier–Stokes equations. We refer to our other works for a detailed description of the mathematical setup^{28,29}. The optimal control problem is solved using a quasi-Newton method. Gradients are derived using adjoint calculus.

The capabilities of our approach are demonstrated using two test cases: The first one is a simple but intriguing demonstration to introduce the concept. Here we consider a wetting and receding droplet on a horizontal surface. The second, more complex example is inspired by recent works, where the heat transfer into a sliding and pinned droplet is characterised², and where drops are trapped due to steep changes in the contact angle³⁰. We assume, that our approach and demonstration initiates further research on optimal control of droplet-based microfluidics.

The remainder of the paper is structured as follows. We discuss the control problems and our proof-of-concept. It follows a description of the control and the optimization problem in and the forward model. Afterwards, some details about the implementation and calculation are given. Finally, we present the results of the multiple control problems including the sliding droplet. A summary and conclusion is the subject of the last section.

Description of Test Cases

To show the applicability of our approach, we consider several optimal control problems. Thereby, we always aim to optimize both the shape and position of the droplet over a given

time horizon.

Droplet on a Horizontal Surface

We start by revising one of the most simplest but still highly intriguing demonstrations of electrowetting. The simplified setup is shown in Figure 1. A single droplet is placed on a horizontal surface with an equilibrium contact angle of $\theta_{eq} = 90^\circ$. The solid and dashed line represent the initial and desired shape and position of the droplet. The control patches, or electrodes, below the surface are used to dynamically change the actual contact angle θ . In this way, the spreading length of the cap-shaped droplet can be precisely adjusted. In an optical application for example this could lead to a modulation of the refractive power. A further example would be the adaption of the heat transfer from the solid surface into the droplet. As we are not concerned here with the technical implementation of the contact angle modification we refer to the recent text book by Mugele and Heikenfeld for an extensive description³¹.

Adjusting the voltage in the patches until the droplet reaches a specific shape and position just by trial-and-error and experience can be cumbersome. This is especially true in complex applications where inertial forces of the droplet or the surrounding phase might lead to ripples or instabilities. Therefore we do not directly specify a contact angle θ to enforce a specific shape of the droplet. In fact, we directly incorporate the desired shape and position of the droplet into an optimal control problem.

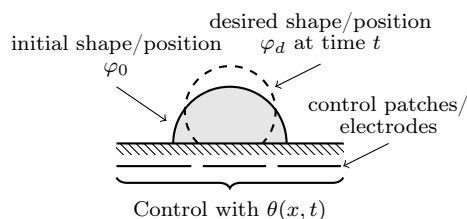


Figure 1: Illustration of the optimal control problem of the symmetric, cap-shaped droplet on a horizontal surface.

Pinning a Sliding Droplet

The example above can be extended to numerous more complex applications. Exemplarily, we discuss a liquid droplet placed on an inclined solid surface. This example is inspired by works, where the heat transfer into a sliding and pinned droplet is characterised², and where drops are trapped due to steep changes in the contact angle³⁰. Here, we want to accomplish a similar pinning of the droplet, i.e., we want to specify a desired position of the droplet. In addition, we want the droplet to have a specific shape at a specific instance in time. In Figure 2, the general physical setting of the problem is illustrated. A single droplet (solid line) is placed on an inclined surface with an equilibrium contact angle of $\theta_{eq} = 90^\circ$. The dashed line represents the desired shape and position at some instance in time. It is clear, that if no control action is taken, the droplet will slide down the surface driven by gravity. However, with the help of the patches u_1 to u_4 we want to control the advancing and receding contact angles θ_1 and θ_2 while the droplet slides along the surface. In this way, we would be able to impose the desired shape and position at a specific time t (light gray).

Apparently, it would be highly cumbersome to find control actions for the patches u_1 to u_4 by extensive trial-and-error. Furthermore, no guarantee can be given, that the control action based on experience would be in some sense optimal. Again we formulate an optimal control problem and incorporate the desired shape into the optimization functional.

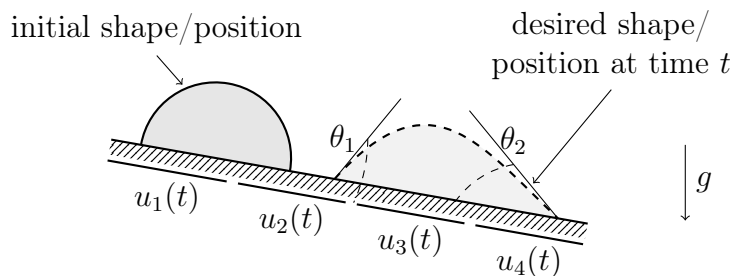


Figure 2: Physical setting of the optimal control problem.

Control Actions

Four different types of control actions will be discussed in this work. We start with the most simplest type and successively approach the proof-of-principle of an optimal control of both the shape and position of a droplet.

A: Constant in Space and Time In this setting, the control is given by one contact angle, that is constant with respect to space and time.

B: Spatially Adapted Here, we separate the surface into equally distributed stripes (or electrodes) and solve the optimal control problem. Each strip can feature a different but constant contact angle. Again, as the contact angles are constant in time (but not in space), we aim to calculate the optimal design of a surface.

C: Temporal Switchable For the next step we consider a real active control problem. That means, that this result can not be implemented in applications without some kind of active control mechanism like electrowetting. In this example, we allow the spatially homogeneous contact angle to switch at a few discrete instances in time. This correspondences to electrowetting with a single electrode.

D: Changeable in Space and Time Finally, we consider the most general optimal control problem. This in fact is needed to consider the sliding droplet case. Therefore, we combine the second and third example. The surface is separated into equally distributed stripes. Each stripe is allowed to switch its contact angle at a few discrete instances in time.

In the following we consider the control actions A and B as passive controls or manufactured controls, because the control action is predefined offline by the manufacturing of the solid surface, while we call the control types C and D as active controls, as they are applied online, while the actual dynamics happens.

Construction of the Design/Control

In this section, we describe the optimization problem that we investigate to obtain optimal controls, i.e. optimal distributions of contact angles with respect to time and space. The following modeling is independent of the actual description of the droplet. We only assume, that there is some measure to quantify the quality of a droplet with respect to some objective. We give examples at the end of this section. We also refer to our complementary works for an extensive description of the mathematical details^{28,29}.

We assume, that we can influence the contact angle at the contact line with a suitable control mechanism (i.e., electrowetting). To state the optimal control problem that defines our controller, we assume, that we have some general description φ of the droplet. The actual description of the droplet, i.e., its full position and shape, is defined and calculated by the utilized forward model. Possible options contain a level set function or a phase-field representation. Moreover, we have some abstract control variable u together with an embedding operator B such that Bu models the actual applied distribution of contact angles in space and time. We finally assume, that for any control u we can calculate a droplet $\varphi(u)$ utilizing some kind of forward model. The considered optimal control problem is given as

$$\min_{\varphi, u} J(\varphi, u) = \frac{1}{2} \int_0^T \int_{\Omega} \omega(t) |\varphi(t, x) - \varphi_d(t, x)|^2 \, dx \, dt + \frac{\alpha}{2} \int_0^T \int_{\partial\Omega} |(Bu)(t, x)|^2 \, dx \, dt$$

(P)

subject to $\varphi = \varphi(u)$,

$$\cos \theta_{\max} \leq Bu + \cos(\theta_{eq}) \leq \cos \theta_{\min},$$

where φ_d represent the desired shape and position of the droplet, $\alpha > 0$ denotes a chosen regularization parameter and θ_{eq} is the equilibrium contact angle of the solid surface without any control action. The actual objective that we encode in the first addend of J is the tracking of a given evolution φ_d over the time horizon $[0, T]$ in the least-squares sense by minimizing their mismatch. We additionally add a time depending weight $\omega(t) \geq 0$ that can be used to pronounce the mismatch in some parts of the time horizon. The second addend

penalises strong control actions and can be used to minimize the controller energy. The angles $0 < \theta_{\min} < \theta_{\max} < \pi$ are given minimum and maximum contact angles. Note that cosine is monotonically decreasing in this range, which leads to the unexpected direction of the inequalities. This can encode physical restrictions, i.e., the contact angle can not be negative, or technical issues, i.e., the control system or technique can not reach contact angles above a certain value. We have chosen this constraint to closely resemble the Young-Lippmann equation for basic electrowetting³¹. For example, if electrowetting is applied to manipulate the contact angle, the maximum accessible contact angle is equal to the equilibrium contact angle. Note, that the precise form of this objective J is not important for the conceptual approach and one might use other models to quantify the quality of a given droplet or include further restrictions. For a general introduction into the field of optimization with constraints given by partial differential equations we refer to^{32,33}.

Model for Control Action u

We model the control Bu by a linear combination of fixed and given control actions. Here the control variable $u = (u_{rs})_{r=1, \dots, R}^{s=1, \dots, S}$ represents the amplitudes of R given control actions $(g_r(t))_{r=1}^R$ that purely depend on time and S control actions $(f_s(x))_{s=1}^S$ that purely depend on space. We use the model

$$(Bu)(t, x) = \sum_{r=1}^R \sum_{s=1}^S u_{rs} g_r(t) f_s(x). \quad (1)$$

In this way we can describe the four settings (A–D) under consideration. To model the setting A we use $R = 1$, $g_1(t) = 1$, and $S = 1$, $f_1(x) = 1$, such that $Bu(t, x) = u_{11}$ describes a constant contact angle in time and space. For the setting B, i.e. controls that depend on space, but that are constant in time, we use $R = 1$, $g_1(t) = 1$ and $S \geq 1$, while the setting C, i.e. the same contact angle on the whole boundary, that might change over time, we use $R \geq 1$ and $S = 1$, $f_1(x) = 1$. Finally, for setting D we use $R \geq 1$ and $S \geq 1$.

Moreover, we only consider controls, that are piecewise constant with respect to time and space, respectively. Thus if we use S controls over the time horizon T , we use $g_s(t) = \chi_{I_s}$. Here, χ_{I_s} denotes the indicator function of the interval $I_s = (\frac{s-1}{S}T, \frac{s}{S}T]$, i.e. $\chi_{I_s}(t) = 1$ if $t \in I_s$ and $\chi_{I_s}(t) = 0$ if $t \notin I_s$. The same structure is used with respect to space.

Modelling the Dynamics and Shape of the Droplet φ

In general, we can apply every model which provides the dynamic position and shape of the droplet in sufficient accuracy as well as the gradient for the optimization to calculate optimal controls. Droplets and curved interfaces in the relevant physical sizes of nanometers to millimeters are most often described by either the lattice Boltzmann model³⁻⁶ or continuum models based on the Navier–Stokes equations^{5,20,27} or simplifications, i.e., thin-film equations. The models can contain expansions to cope with additional difficulties like contact angle hysteresis³⁴, or electrostatics³¹. The representation of the gas-liquid interface in continuum models can be further subdivided into sharp and diffuse interface methods. For an in-depth description of these methods we refer to the review by Wörner³⁵.

In the following, we apply a diffuse interface model based on the Cahn–Hilliard–Navier–Stokes (CHNS) equations. In contrast to many other methods, the Cahn–Hilliard equation allows the contact line to move naturally on the solid surface due to a diffusive flux across the interface even if no-slip is assumed³⁶. As summarized in the review by Wörner, the Cahn–Hilliard–Navier–Stokes (CHNS) equations can easily handle topological changes of the interface (merging and breakup)³⁷, the contact line can be accurately represented³⁸ and the interface is implicitly tracked without any prior knowledge of the position. Furthermore, one of the major advantages is, that the formulation of the surface tension force in the Navier–Stokes (NS) equation exactly conserves both the surface tension energy and kinetic energy. This can reduce spurious currents, which are purely artificial velocities around the interface, to the level of the truncation error even for low Capillary numbers^{39,40}. The droplet is described by a smooth indicator function that can be directly used in (P). In the following,

we give a brief introduction of this model. Further details about the gradient of our model needed in the optimization routine we refer to our recent work²⁹.

Forward Model

In this section, we introduce the model for the evolution of the droplet that is used throughout this work. We consider a phase field model, coupling the incompressible Navier–Stokes equations with the Cahn–Hilliard equation^{36,41,42}. Compared to sharp interface methods, phase field methods replace the infinitely thin layer (interface) between gas and liquid by a transition region with positive thickness. Moreover, they describe the distribution of the different fluids by a smooth indicator function (phase field) and do not explicitly involve the location of the transition region. It follows, that all physical properties like density or viscosity vary continuously across the interface and can be described in terms of the phase field.

The liquid droplet and the surrounding air are modeled as Newtonian, isotherm, immiscible and incompressible fluids. In this work, the common incompressible, single-field Navier–Stokes (NS) equation is combined with the convective Cahn–Hilliard (CH) equation to describe the interface dynamics. To describe the spatial distribution of the two phases (liquid and gas) with a single variable, an order parameter or phase field φ is introduced as

$$\varphi(x, t) = \begin{cases} -1 & \text{for pure phase 1 at } (x, t), \text{ called } \textit{gas} , \\ +1 & \text{for pure phase 2 at } (x, t), \text{ called } \textit{liquid} . \end{cases} \quad (2)$$

Note that this method postulates the existence of a diffuse interface Γ_ϵ between the two phases where both phases are present. In this region $\varphi \in (-1, 1)$ holds. See Figure 3 for a sketch of φ . Since φ is assumed to be continuous across the diffuse interface, we can interpret its zero-level line as a sharp separation line between gas and liquid and use this line

to present numerical results. Finally we stress, that φ is the outcome of the forward model and its structure is thus generated by the forward model. The further primal variables are

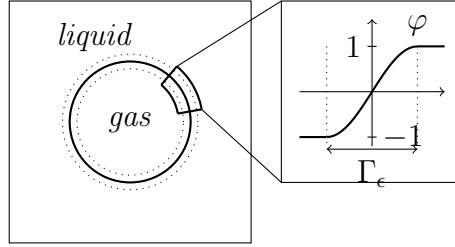


Figure 3: A sketch of the phase field approach. On the left, the two-phase distribution with gas and liquid phase is depicted together with the diffuse interface that separates the two phases, indicated by the dotted lines. On the right, a blow-up of φ across this interface Γ_ϵ . We have $\varphi = 1$ in the liquid phase and $\varphi = -1$ in the gas phase.

given by the velocity field v , the pressure field p , and the chemical potential μ . In this work a thermodynamically consistent diffuse interface model for large density differences between gas and liquid⁴¹ is applied

$$\rho \partial_t v + (\rho v + J) \nabla v - \operatorname{div}(2\eta Dv) + \nabla p = -\varphi \nabla \mu + \rho g, \quad (3)$$

$$-\operatorname{div}(v) = 0, \quad (4)$$

$$\partial_t \varphi + v \nabla \varphi - b \Delta \mu = 0, \quad (5)$$

$$-\sigma \epsilon \Delta \varphi + \frac{\sigma}{\epsilon} W'(\varphi) = \mu, \quad (6)$$

which is closed with the initial data and boundary conditions^{42,43},

$$v(t=0) = v_0, \quad v = 0 \quad \text{on } \partial\Omega, \quad (7)$$

$$\varphi(t=0) = \varphi_0, \quad \sigma \epsilon \nabla \varphi \cdot \nu_\Omega + \gamma'_u(\varphi) = 0 \quad \text{on } \partial\Omega, \quad (8)$$

$$\nabla \mu \cdot \nu_\Omega = 0 \quad \text{on } \partial\Omega, \quad (9)$$

where ν_Ω denotes the outer unit normal on the computational domain. We use the abbreviations $J := -b \frac{\partial \rho}{\partial \varphi} \nabla \mu$, where b denotes the constant mobility in the Cahn–Hilliard model to be explained below, and $2Dv := \nabla v + (\nabla v)^t$. The gravitational acceleration is denoted

by g and $p = p^{phys} - \mu\varphi$ is a shifted pressure, where p^{phys} denotes the physical pressure. The density function is denoted by $\rho \equiv \rho(\varphi) > 0$ and satisfies $\rho(-1) = \rho_g$ and $\rho(1) = \rho_l$, with ρ_g, ρ_l denoting the constant densities of the two involved fluids, i.e. gas and liquid. It is a linear function with respect to φ . The viscosity function is $\eta \equiv \eta(\varphi) > 0$ and satisfies $\eta(-1) = \eta_g$ and $\eta(1) = \eta_l$, with η_g, η_l denoting the viscosities of the involved fluids. Here, ρ and η are given by

$$\rho(\varphi) := \frac{\rho_l + \rho_g}{2} + \frac{\rho_l - \rho_g}{2}\varphi, \quad \eta(\varphi) := \frac{\eta_l + \eta_g}{2} + \frac{\eta_l - \eta_g}{2}\varphi. \quad (10)$$

In summary, (3)–(4) describe the Navier–Stokes equation with a spacially varying density ρ and a spacially varying viscosity η . Thus we use one model to describe the velocity in both gas and liquid. Additionally there appear two non-standard terms. The first is the small additional flux J that stems from additional transport that is introduced by the diffuse interface method. The second is the term $\varphi\nabla\mu$ that is a model for the interfacial forces stemming from surface tension σ between liquid and gas. Notice that the variable μ scales with σ , which can be seen by investigating (6).

The function $W(\varphi)$ denotes a dimensionless potential of double-well type with two minima at $\varphi = \pm 1$. Here, we choose

$$W(\varphi) := \begin{cases} \frac{1}{4}(1 - \varphi^2)^2 & \text{if } |\varphi| \leq 1, \\ (|\varphi| - 1)^2 & \text{else,} \end{cases} \quad (11)$$

see Figure 4. This term leads to the phase field structure of the phase field φ with its distinct values $\varphi = \pm 1$ for the pure phases.

The constant $\sigma = c_W\sigma_{lg}$ denotes the surface tension between liquid and gas, where σ_{lg} denotes the physical value of the surface tension and the constant c_W is a necessary scaling of the physical surface tension that appears from the diffuse interface approach. For the potential (11) c_W is given by $c_W = \frac{3}{2\sqrt{2}}$ ⁴⁴. The constant ϵ is proportional to the thickness

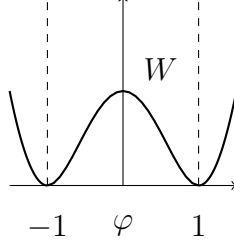


Figure 4: The double-well potential W .

of the diffuse transition zone between gas and liquid. For $\epsilon \rightarrow 0$, i.e. if the transition zone between gas and liquid becomes small, at least formally a consistent sharp interface model can be recovered^{41,45}. Finally the constant $b = m\epsilon$, $m > 0$ denotes the constant mobility of particles in the Cahn–Hilliard equation with transport (5)–(6).

In the Cahn–Hilliard equation, the phase field evolves by two flux processes, namely it is transported by the velocity field v which is described by the term $v\nabla\varphi$ and additionally by its intrinsic flux $b\nabla\mu$. The latter is a flux, that tends to minimize the curvature of the interface between the two phases. The Cahn–Hilliard equation without transport is commonly derived as a mass-conserving gradient flow that minimizes the length of the interface between gas and liquid.

Finally, the wall potential is denoted by γ and interpolates smoothly between the solid-liquid and solid-gas surface energies. The expression for γ is given by

$$\gamma_u(\varphi) = \frac{\sigma_{sl} + \sigma_{sg}}{2} + \sigma_{gl}(\cos \theta_{eq} + Bu)\vartheta(\varphi) \quad (12)$$

where ϑ is a smooth monotonically increasing function with $\vartheta(-1) = -\frac{1}{2}$ and $\vartheta(1) = \frac{1}{2}$ such that $\gamma_u(-1) = \frac{1}{2}(\sigma_{sl} + \sigma_{sg} - \sigma_{gl}(\cos \theta_{eq} + Bu)) = \sigma_{sg}$ is satisfied by Young’s law, i.e. $\sigma_{sl} - \sigma_{sg} = \sigma_{lg}(\cos \theta_{eq} + Bu)$, and $\gamma_u(1) = \sigma_{sl}$ holds by the same arguments. Here θ_{eq} denotes the static equilibrium contact angle between the solid and the interface and is measured in the liquid phase, while σ_{sg} denotes the surface tension between solid and gas, and σ_{sl} denotes the surface tension between solid and liquid. Further, Bu denotes some change of the contact angle due to the applied control. Note the close resemblance of our formulation

of (12) and the Young-Lippmann equation for basic electrowetting³¹. It follows, that the calculated controls u can be readily implemented in electrowetting devices.

Finally we note, that an expression for ϑ can for example be derived based on the assumption of equipartition of energy, i.e., $\frac{\epsilon}{2}|\nabla\varphi|^2 \approx \frac{1}{\epsilon}W(\varphi)$ ⁴⁶. This leads to $\vartheta'(\varphi) = c_W\sqrt{2W(\varphi)}$. In Figure 5 we depict the local situation at the contact line and show a sketch of γ_u . The boundary data (8) models a static contact angle of θ_{eq} , for simplicity. This can be extended to contain contact line hysteresis⁴⁴.

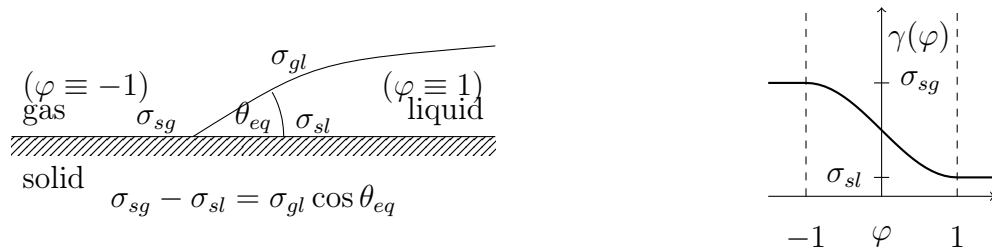


Figure 5: The local situation at the contact line, including Young's law on the left. On the right a sketch of γ across the interface.

For further details about the model as well as different bulk and wall potentials we refer to Bonart et al.⁴⁴. Applications of the model include rising bubbles^{44,47}, the pinning of droplets⁴⁸, and thin liquid films⁴⁹. Especially for a comparison with sharp interface simulations and experimental measurements without contact line motion, see⁵⁰.

The model (3)–(6) can be derived purely from thermodynamic principles^{41,42}. Here it is postulated, that the system in the whole domain Ω with boundary $\partial\Omega$ can be described by the following sum of kinetic energy and Helmholtz free energy functional of Ginzburg–Landau type⁵¹

$$E = \frac{1}{2} \int_{\Omega} \rho |v|^2 \, dx + \sigma \int_{\Omega} (\epsilon^{-1}W(\varphi) + \epsilon|\nabla\varphi|^2) \, dx + \int_{\partial\Omega} \gamma \, ds. \quad (13)$$

Note that the second integral can be shown to relate to the length of the interface between liquid and gas.

Numerical Implementation and Solution

For the solution of the optimization problem (P) we apply the software IPOPT⁵². To utilize the efficient, gradient-based quasi-Newton method in IPOPT, we require the evaluation of the gradient of J . Here we use adjoint calculus to efficiently evaluate this object^{32,33}. In turn, evaluation of the gradient requires one solve of the forward model and additionally the evaluation of the so called adjoint equation. The adjoint and the gradient for (P) are derived using standard methods from adjoint calculus and follow directly from the discrete forward model and the functional. We refer to^{29,53} for the model-specific mathematical details. Note, that the problem (P) is non-convex. As common for these type of optimization problems we can only expect to achieve a local minimizer and multiple solutions in dependence on the initial guess are possible.

For the numerical implementation and solution of the forward and adjoint models we apply the finite element package FEniCS 2019.1.0^{54,55}. See our recent works for a discussion of numerical schemes to solve the forward model (3) – (6)^{29,44}. For the solution of the arising linear systems and subsystems the software suite PETSc 3.8.4^{56–58} is used. Common for Newton-based methods, the optimization is conducted iteratively. In every step, we have to solve the forward and adjoint model to calculate the gradient. Note, that almost all the computing time is spend in the solution of the forward and adjoint models. Therefore, the total calculation time needed for the optimization greatly depends on highly optimized solution strategies for the forward model and the adjoint equation. Our results were calculated on simple workstations utilizing only a single core and took at most four hours to finish.

Optimal Control of Droplets

In this section we demonstrate the applicability of our approach and framework. At first, the general setup is described. Then we describe the results for the design cases A and B as well as the active control cases C and D. Finally, we extend the first example to sliding

droplets. Especially, for the pinning of the sliding droplet the most complex case D with its spatial and temporally varying contact angles is vital.

General Setup

Table 1 states the physical and numerical parameters applied throughout this section. Exemplarily, we used a water droplet with a diameter $l_d = 5$ mm surrounded by air on a solid surface with $\theta_{eq} = 90^\circ$. The time step was set to $\tau = 0.001$ s. An adaptive mesh was utilized so that the interface between gas and liquid was resolved with at least four cells at all times ($h_{min} = 0.04$ mm).

Table 1: Physical and numerical parameters of droplet (water), surrounding gas (air) and solid surface.

l_d/mm	$\sigma_{gl}/\text{mN m}^{-1}$	$\rho_l/\text{kg m}^{-3}$	$\eta_l/\text{mPa s}$	$\rho_g/\text{kg m}^{-3}$	$\eta_g/\text{mPa s}$	$g/\text{m s}^{-2}$	$\theta_{eq}/^\circ$
5	72.86	998	1.0	1.2	0.018	9.81	90
ϵ/mm	$b/\text{m}^3 \text{J}^{-1} \text{mm}^2 \text{s}^{-1}$	τ/s	h_{min}/mm				
0.2	0.04	0.001	0.04				

The desired shapes φ_d were created by simulating the forward model (3)–(6) from a suitable initial value, which is specified for the individual setups, until the equilibrium droplet shape was reached.

The values of R and S for the four control cases are given in Table 2 for the two numerical examples. In both examples the stripes as well as the switching points were equally distributed over the length of the bottom wall and the time horizon of $I = [0.0, T]$ with $T = 1$ s, respectively.

The weight ω was chosen as

$$\omega(t) = \begin{cases} 1 & \text{if } t \in (0, 0.8)\text{s}, \\ 10^5 & \text{if } t \in [0.8, 1.0]\text{s}, \end{cases} \quad (14)$$

to promote a good matching of φ and φ_d at the end of the optimization horizon between 0.8 s and 1.0 s. Note, that the high value of the weight is quite arbitrary and setting smaller values results in almost the same controls. We stopped the optimizer as soon as the initial gradient ∇J was reduced by a factor of $\frac{1}{100}$.

Table 2: Values of R and S for the control cases A to D for both problems.

	Prob. 1				Prob. 2
	A	B	C	D	D
R	1	1	5	5	10
S	1	5	1	5	10

Droplet on a Horizontal Surface

At first, we report on the optimal control of the first example. The domain was of dimension $\Omega = l_d \times l_d$ and we made use of the symmetrical droplet. In this way, we assumed symmetric conditions at the left side of the domain and solid walls at the top, bottom and right side of the domain. The bottom wall contained the control of the contact angle. The desired shape φ_d with an equilibrium contact angle of 135° is shown as the dashed line in Figure 6. In the first row of Figure 6 the initial droplets with $Bu = 0$ and $\theta_{eq} = 90^\circ$ are shown. The values for R and S for the control cases are given in Table 2. In this example, at most five stripes with each five switching points in time were considered.

We discuss the following aspects of our numerical results:

Resulting Droplet Shapes The droplet shapes calculated with the resulting optimal control values Bu for the cases A to D are depicted in Figure 6. The solid lines represent the isolines where $\varphi = 0$. We show the shape and position of the droplet at five instances in time. Note, that only the relevant clipping of Ω is displayed in Figure 6.

Relative Mismatch The relative mismatch between the actual droplet and the desired shape over time,

$$\frac{\Delta\varphi(t)}{\Delta\varphi^0} = \sqrt{\frac{\int_{\Omega}(\varphi(t) - \varphi_d)^2 dx}{\int_{\Omega}(\varphi^0 - \varphi_d)^2 dx}}, \quad (15)$$

which is normalized with the mismatch at $t = 0.0$ s, is displayed in the top part of Figure 8.

Optimal Controls The corresponding optimal controls Bu for the cases A to D are plotted in Figure 7. In the first two columns the controls are constant in time, whereas the controls are constant in space in the first and third column. The dashed lines represent the control which was used to create the desired shape φ_d (i.e., $\cos(135^\circ) \approx -0.7071$).

Relative Controller Strength The relative controller strength per time interval r is calculated with

$$\frac{E_r}{E_A} = \frac{\frac{1}{S}\sqrt{\sum_{s=1}^S u_{rs}^2}}{|u_A|}. \quad (16)$$

The control strength per time interval is normalized to the (constant) control strength needed in case A. We further assume, that the control costs scale linearly with the length of the control domain, which leads to the normalization with $\frac{1}{S}$ in the numerator. It is plotted in the lower part of Figure 8.

Cases A and B

Comparing the design cases A and B (first and second column in Figure 6) it is evident that the droplet behave almost identical: the shapes and the positions of the contact lines are very similar. The desired shape is reached with very high accuracy after a short time (see $t = 0.4$ s) in both cases. The mismatches $\Delta\varphi$ displayed in the top part of Figure 8 (solid lines with triangular and circular markers) decline with the same slope over time and reach

almost zero at around $t = 0.4$ s.

Now we focus on the first and second column of Figure 7 to include the optimal controls into our discussion. In case A we only allowed for a single control action for the whole surface and time horizon. Subsequently, only one value is displayed in column one. As expected from the shape of the droplet, the control value is very close to the value which was used to create the desired droplet φ_d , see the dashed line in the lower left panel of Figure 7.

In case B the stripe between 2 mm and 3 mm has a control value which is slightly lower than the equilibrium value obtained again in the stripe $[1, 2]$ mm. This results in a more rapid receding of the droplet on that stripe in case B. However, as the droplet spends only little time on that stripe the influence on the overall dynamics of the droplet are low. Since in case B only a portion of the bottom controls are active at any time, the controller strength is significantly lower compared to case A, see the lower part of Figure 8.

Cases C and D

From comparing the shape of the droplets in the active cases C and D (third and fourth column in Figure 6) we again notice that the droplets behave almost identical: the shapes and the positions of the contact lines are very similar. The desired shape is reached relatively late but still a very high accuracy after $t = 0.8$ s in both cases. This stems from the weight ω defined above, which was strongly penalizing the interval $[0.8, 1.0]$. Before 0.6 s the droplets do not move at all. This can be seen by looking at the mismatches of φ displayed in the top part of Figure 8 (solid lines with rectangular and open circular markers). Until 0.6 s the mismatch gets even higher than the initial mismatch. This is due to the initial droplet adapting to gravity. The subsequent decline however is very rapid and happens with almost the same slope over time for the cases C and D. Finally, it reaches a small value at around $t = 0.8$ s.

By investigating the controls in the third and fourth column of Figure 7 the explanation for the observed droplet shapes becomes obvious. In the first three intervals the control

action is approximately zero. Only for the last intervals control actions are needed to reach the desired shape in time. This leads to very low relative controller strengths required to reach the optimization target, see the lower panel of Figure 8. The most complex control sequence is calculated in case D. Here, the droplet moves in a very versatile and controlled fashion until it reaches the desired shape with a very low relative controller strength.

For all cases A to D we were able to calculate optimal controls to reach the desired shape for a specific time interval: the shapes of the droplets match the desired shape in all cases almost perfectly (Figure 6) and the mismatch gets very low (Figure 8, top). In cases C and D, the mismatch decreases slower than in cases A and B. This indicates, that a shorter time horizon would be sufficient for the control task. In all cases the final control values for the stripe between 1 mm and 2 mm is almost the same as the one used for the desired shape (Figure 7). This is expected, since the desired shape is stable situation with a constant contact angle. Moreover, the final contact point is located in this stripe, thus defining the shape of the droplet. Subsequently, the required relative controller strengths in the cases C and D are much smaller than in the cases A and B (Figure 8, bottom). This is due to the fact, that the more complex controls can act more locally precise with respect to space and time. Thus they are not active (i.e. $Bu = 0$) in large parts of the spatial and temporal domain.

Pinning a Sliding Droplet

To demonstrate the general applicability of our approach we extend the example discussed above to the optimal pinning of a sliding droplet. The pinning of a sliding droplet at a specific position on a solid surface while maintaining a desired shape can have interesting implications for technical applications. At the same time, this is a challenging task.

The domain was of dimension $\Omega = 2l_d \times l_d$. We assumed symmetric conditions at the left side of the domain and solid walls at the top, bottom and right side of the domain. The inclined bottom wall contained the control of the contact angle. The inclination of the plate

was 45° to the horizontal. Exemplary, we used the dashed line in Figure 9 as the desired shape φ_d at this position on the inclined surface. The desired droplet was produced by simulating the forward model from a cap-shaped droplet at $(x, y) = (1.25l_d, 0)$ with $Bu = -0.7071$ and $\theta_{eq} = 90^\circ$. In the first row of Figure 9 the initial droplets at $t = 0$ and $(x, y) = (0.75l_d, 0)$ with $Bu = 0$ and $\theta_{eq} = 90^\circ$ are shown. The values for R and S are given in Table 2. We considered ten stripes with each ten switching points in time. The stripes as well as the switching points were equally distributed over the space of 10 mm and the time horizon of 1 s.

Note, that a steady droplet with the desired shape on the inclined surface under the influence of gravity is physically impossible. However, in this example, we just want to enforce an as symmetrical droplet as possible at a specific time and location on the inclined surface. It follows, that the droplet by no means has to be in equilibrium and steady at the final time. We have specifically chosen this example to demonstrate the, sometimes surprising, capabilities of optimal active control. Specifying a desired droplet which is physically in equilibrium would not require active control but merely the design of a patterned wettability of the surface.

No Control At first we show the droplet sliding down the inclined surface without any control at all ($Bu = 0$ for all times), see the first column in Figure 9. Secondly, one might naively set the control to the finally desired contact angle of 135° . This is displayed in the second column. In both cases the droplet is far from the desired shape as well as the desired position at the specified time. It is clearly evident that finding the right control actions by trial-and-error might be certainly cumbersome. Furthermore, we do not only want to obtain any controls but the controls which minimize the functional (P).

Optimal Control In the third column of Figure 9 the droplet's isolines calculated from the optimal control action are displayed. We notice, that in the optimal case we match the desired shape at the desired position very well between 0.8 s and 1.0 s. Comparing this to the

naive approaches with $Bu = 0$ and $Bu = -0.7071$ the improvement is tremendous. During the sliding and pinning the droplet exhibits multiple surprising shapes resulting from the strong impact of the control actions on the droplet. The control actions are needed due to the desired shape being far from the steady shape of a droplet in equilibrium on an inclined surface.

The control actions Bu in each time interval are shown in the last column of Figure 9. It is striking how complex these optimal controls Bu are. We would have found this very difficult and costly to find this control action by trial-and-error. While pulled by gravity, each of the droplet's contact points are forced to recede and spread multiple times. See for example between 0.4 s and 0.6 s the stripes between 1 mm to 2 mm and 7 mm to 8 mm. The control action jumps from between large and small values, which leads to the pinning of the contact points.

Discussion and Conclusion

In this work we demonstrated for the first time some capabilities of optimal control of both the shape and position of a droplet. Therefore, we considered the active control of a sliding droplet using temporally and spatially varying optimal contact angle distributions. In this basic example common for droplet-based microfluidics the droplet slides on an inclined surface and gets pinned at a specific position with a desired shape. We specifically chose a desired shape which is far from the steady shape of a droplet on an inclined wall in equilibrium. In our demonstration, the position and shape of the droplet matched the desired properties very well. The dynamics of the droplets were calculated using a phase field model. We solved the optimal control problem using a quasi-Newton method. The gradients were calculated using the adjoints. The resulting controls were profoundly complex and would not have been found by trial-and-error.

Our work indicates that optimal control of droplets or curved interfaces is feasible and

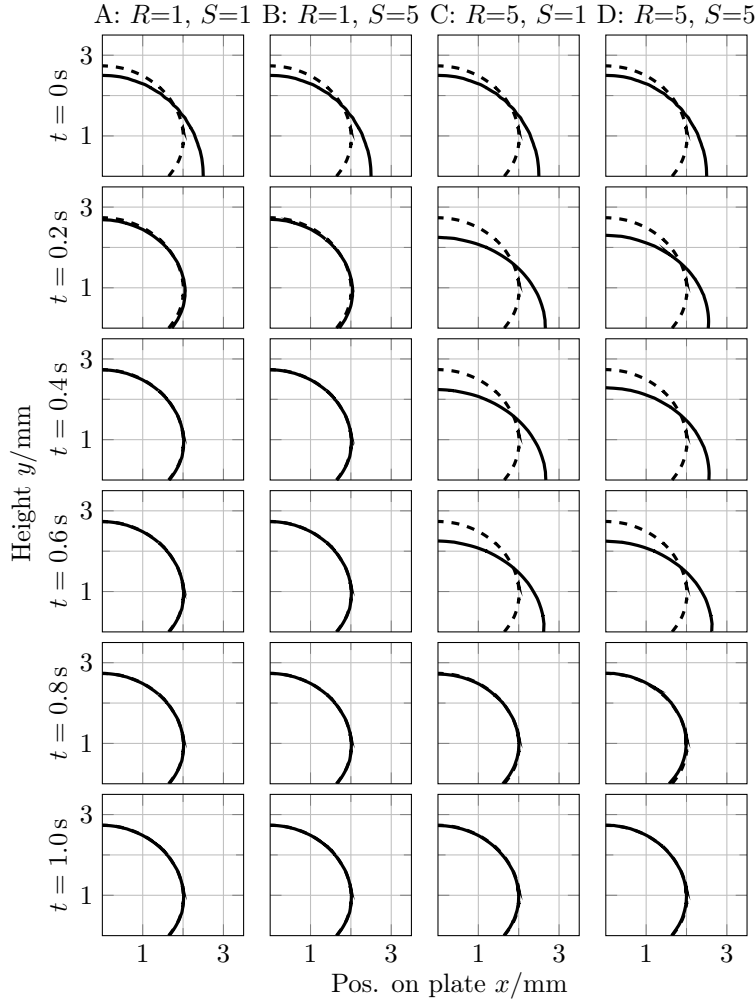


Figure 6: Development of the receding droplets over time for the optimization cases A to D. Due to the symmetric droplet only the right half of the isoline for $\varphi = 0$ is displayed. The desired shape and position of the droplet φ_d is included as the dashed line.

allows for interesting applications. This includes to utilize optimal control in highly precise optofluidic applications¹³ or microfluidic devices⁵⁹ Two main challenges have to be tackled for this kind of optimal control applications. The first one is the prediction of the shape and position of the curved interface with sufficient accuracy. The second challenge is posed by the calculation time required for the forward and adjoint model. The calculation is computationally very expensive and takes most of the time during the optimization. Furthermore, it depends on the required accuracy, e.g., time step width or grid size.

We showed, that the offline calculation of optimal control strategies and designs is already

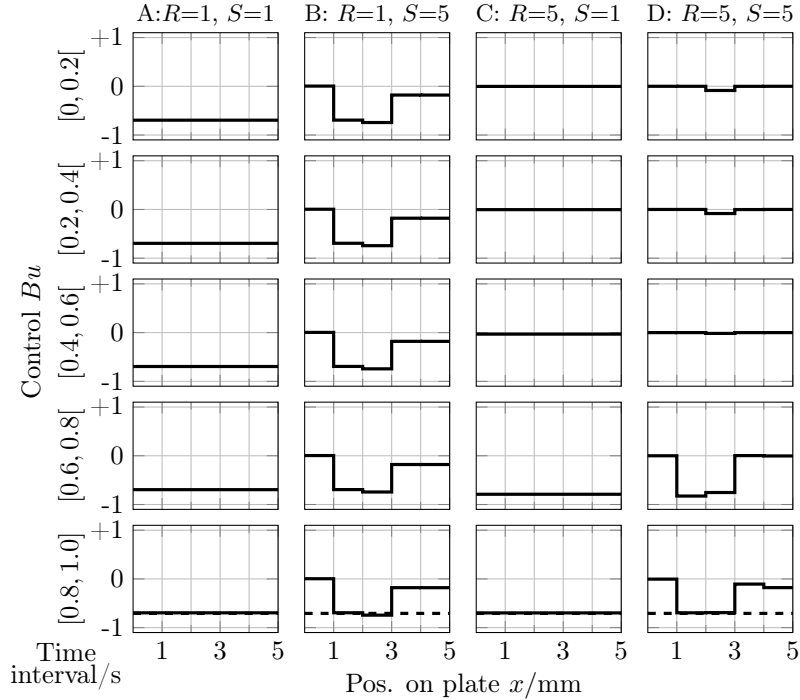


Figure 7: Development of the controls over time for the optimization cases A to D. Due to the symmetric droplet only the right half of the controls is displayed. The control which was used to create the desired droplet φ_d is displayed as the dashed line at the bottom row.

feasible while using the highly-accurate forward model based on the Cahn–Hilliard–Navier–Stokes equations together with the gradient-based optimization strategy. Even more precise representations of the droplet or curved interface do not change the proposed optimal control methods. This allows for example to account for contact angles hysteresis by adapting the forward model. However, for the precise online control including a feedback loop and droplets in 3D the computational speed is prohibitive. Model-order reduction might be a remedy to speed up the calculation of the forward and adjoint model in 3D.

In order for our proposed approach to inspire new experimental approaches and enable detailed functionalities, more in-depth research is required. This includes the individual aspects of the optimization concept but also the forward modelling and practical demonstrations. For example, by adopting optimal experimental design the number of required control stripes on the surface could be part of the optimization itself. In addition, manufacturing or cost constraints could be included and deliver more practical solutions. In this way, the opti-

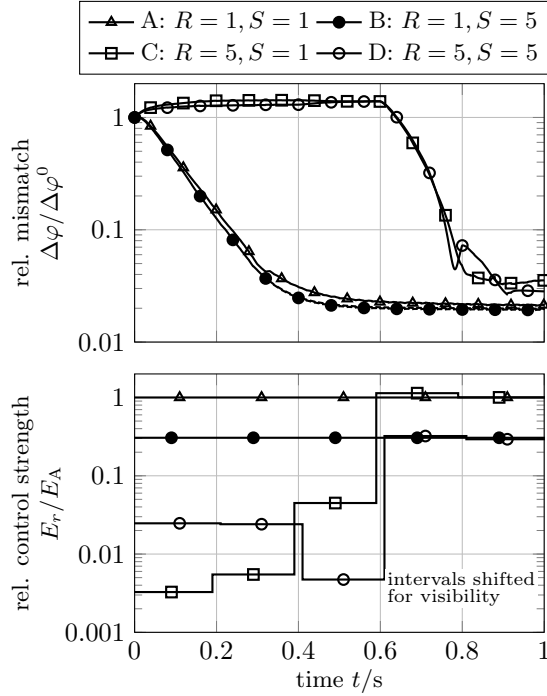


Figure 8: Development of the relative mismatch (top) and the relative control strength for the cases A, B, C and D.

mization could help experimenters in the design of their experimental setups and parameter studies to reduce the cost and time.

Acknowledgments

The first and third author thank the German Research Foundation (DFG) for the financial support within the project RE 1705/16-1.

References

- (1) Pollack, M. G.; Shenderov, A. D.; Fair, R. B. Electrowetting-based actuation of droplets for integrated microfluidics. *Lab on a Chip* **2002**, *2*, 96–101.
- (2) Al-Sharafi, A.; Yilbas, B. S.; Ali, H.; Alaqeeli, N. A Water Droplet Pinning and Heat

- Transfer Characteristics on an Inclined Hydrophobic Surface. *Scientific Reports* **2018**, *8*, 3061.
- (3) Kusumaatmaja, H.; Yeomans, J. M. Controlling drop size and polydispersity using chemically patterned surfaces. *Langmuir* **2007**, *23*, 956–959.
- (4) Jansen, H. P.; Sotthewes, K.; Van Swigchem, J.; Zandvliet, H. J.; Kooij, E. S. Lattice Boltzmann modeling of directional wetting: Comparing simulations to experiments. *Physical Review E - Statistical, Nonlinear, and Soft Matter Physics* **2013**, *88*, 013008.
- (5) Vrancken, R. J.; Blow, M. L.; Kusumaatmaja, H.; Hermans, K.; Prenen, A. M.; Bastiaansen, C. W.; Broer, D. J.; Yeomans, J. M. Anisotropic wetting and de-wetting of drops on substrates patterned with polygonal posts. *Soft Matter* **2013**, *9*, 674–683.
- (6) Varagnolo, S.; Schiocchet, V.; Ferraro, D.; Pierno, M.; Mistura, G.; Sbragaglia, M.; Gupta, A.; Amati, G. Tuning drop motion by chemical patterning of surfaces. *Langmuir* **2014**, *30*, 2401–2409.
- (7) Chen, S.; Cheng, Y.; Zhang, G.; Pei, Q.; Zhang, Y. W. Anisotropic Wetting Characteristics of Water Droplets on Phosphorene: Roles of Layer and Defect Engineering. *Journal of Physical Chemistry C* **2018**, *122*, 4622–4627.
- (8) Wang, Y.; Jian, M.; Liu, H.; Zhang, X. Anisotropic Wetting of Droplets on Stripe-Patterned Chemically Heterogeneous Surfaces: Effect of Length Ratio and Deposition Position. *Langmuir* **2019**, *35*, 4387–4396.
- (9) Yang, C.; Wu, L.; Li, G. Magnetically Responsive Superhydrophobic Surface: In Situ Reversible Switching of Water Droplet Wettability and Adhesion for Droplet Manipulation. *ACS Applied Materials and Interfaces* **2018**, *10*, 20150–20158.
- (10) Plog, J.; Löwe, J. M.; Jiang, Y.; Pan, Y.; Yarin, A. L. Control of Direct Written Ink Droplets Using Electrowetting. *Langmuir* **2019**, *35*, 11023–11036.

- (11) Berge, B.; Peseux, J. Variable focal lens controlled by an external voltage: An application of electrowetting. *European Physical Journal E* **2000**, *3*, 159–163.
- (12) Hou, L.; Smith, N. R.; Heikenfeld, J. Electrowetting manipulation of any optical film. *Applied Physics Letters* **2007**, *90*, 251114.
- (13) Lima, N. C.; Mishra, K.; Mugele, F. Aberration control in adaptive optics: a numerical study of arbitrarily deformable liquid lenses. *Optics Express* **2017**, *25*, 6700.
- (14) Lim, W. Y.; Supekar, O. D.; Zohrabi, M.; Gopinath, J. T.; Bright, V. M. Liquid Combination with High Refractive Index Contrast and Fast Scanning Speeds for Electrowetting Adaptive Optics. *Langmuir* **2018**, *34*, 14511–14518.
- (15) Brzobohatý, O.; Chvátal, L.; Jonáš, A.; Šiler, M.; Kaňka, J.; Ježek, J.; Zemánek, P. Tunable Soft-Matter Optofluidic Waveguides Assembled by Light. *ACS Photonics* **2019**, *6*, 403–410.
- (16) Li, L. Y.; Yuan, R. Y.; Wang, J. H.; Li, L.; Wang, Q. H. Optofluidic lens based on electrowetting liquid piston. *Scientific Reports* **2019**, *9*, 13062.
- (17) Song, X.; Zhang, H.; Li, D.; Jin, Q.; Jia, D.; Liu, T.; Wang, C. Liquid Lens with Large Focal Length Tunability Fabricated in a Polyvinyl Chloride/Dibutyl Phthalate Gel Tube. *Langmuir* **2020**, *36*, 1430–1436.
- (18) Kuiper, S.; Hendriks, B. H. Variable-focus liquid lens for miniature cameras. *Applied Physics Letters* **2004**, *85*, 1128–1130.
- (19) Mishra, K.; van den Ende, D.; Mugele, F. Recent developments in optofluidic lens technology. *Micromachines* **2016**, *7*, 102.
- (20) Armani, M.; Chaudhary, S.; Probst, R.; Walker, S.; Shapiro, B. Control of microfluidic systems: Two examples, results, and challenges. *International Journal of Robust and Nonlinear Control* **2005**, *15*, 785–803.

- (21) Walker, S.; Shapiro, B. A control method for steering individual particles inside liquid droplets actuated by electrowetting. *Lab on a Chip* **2005**, *5*, 1404–1407.
- (22) Niu, X.; Zhang, M.; Peng, S.; Wen, W.; Sheng, P. Real-time detection, control, and sorting of microfluidic droplets. *Biomicrofluidics* **2007**, *1*, 044101.
- (23) Wong, D.; Ren, C. L. Microfluidic droplet trapping, splitting and merging with feedback controls and state space modelling. *Lab on a Chip* **2016**, *16*, 3317–3329.
- (24) Lee, J. H. Model predictive control: Review of the three decades of development. *International Journal of Control, Automation and Systems* **2011**, *9*, 415–424.
- (25) Laurain, A.; Walker, S. W. Droplet footprint control. *SIAM Journal on Control and Optimization* **2015**, *53*, 771–799.
- (26) Antil, H.; Hintermüller, M.; Nochetto, R. H.; Surowiec, T. M.; Wegner, D. Finite horizon model predictive control of electrowetting on dielectric with pinning. *Interfaces and Free Boundaries* **2017**, *19*, 1–30.
- (27) Fumagalli, I.; Parolini, N.; Verani, M. Optimal control in ink-jet printing via instantaneous control. *Computers and Fluids* **2018**, *172*, 264–273.
- (28) Bonart, H.; Kahle, C.; Repke, J.-U. Controlling Sliding Droplets with Optimal Contact Angle Distributions and a Phase Field Model. *Pamm* **2019**, *19*, 10–11.
- (29) Bonart, H.; Kahle, C. Optimal Control of Sliding Droplets using the Contact Angle Distribution. **2020**,
- (30) ’T Mannetje, D.; Ghosh, S.; Lagraauw, R.; Otten, S.; Pit, A.; Berendsen, C.; Zeegers, J.; Van Den Ende, D.; Mugele, F. Trapping of drops by wetting defects. *Nature Communications* **2014**, *5*, 3559.
- (31) Mugele, F.; Heikenfeld, J. *Electrowetting*; Wiley-VCH Verlag GmbH & Co. KGaA: Weinheim, Germany, 2018.

- (32) Tröltzsch, F. *Optimale Steuerung partieller Differentialgleichungen*; Vieweg Verlag: Wiesbaden, 2009.
- (33) Hinze, M.; Pinnau, R.; Ulbrich, M.; Ulbrich, S. *Optimization with PDE Constraints*; Mathematical Modelling: Theory and Applications; Springer Netherlands: Dordrecht, 2009; Vol. 23.
- (34) Eral, H. B.; 'T Mannetje, D. J.; Oh, J. M. Contact angle hysteresis: A review of fundamentals and applications. *Colloid and Polymer Science* **2013**, *291*, 247–260.
- (35) Wörner, M. Numerical modeling of multiphase flows in microfluidics and micro process engineering: A review of methods and applications. *Microfluidics and Nanofluidics* **2012**, *12*, 841–886.
- (36) Jacqmin, D. Contact-line dynamics of a diffuse fluid interface. *Journal of Fluid Mechanics* **2000**, *402*, 57–88.
- (37) Anderson, D.; McFadden, G.; A. A. Wheeler, Diffuse-interface methods in fluid mechanics. *Annual Review of fluid mechanics* **1998**, *30*, 139–165.
- (38) Seppacher, P. Moving contact lines in the Cahn-Hilliard theory. *International Journal of Engineering Science* **1996**, *34*, 977–992.
- (39) He, Q.; Kasagi, N. Phase-Field simulation of small capillary-number two-phase flow in a microtube. *Fluid Dynamics Research* **2008**, *40*, 497–509.
- (40) Jamshidi, F.; Heibel, H.; Hasert, M.; Cai, X.; Deutschmann, O.; Marschall, H.; Wörner, M. On suitability of phase-field and algebraic volume-of-fluid OpenFOAM® solvers for gas-liquid microfluidic applications. *Computer Physics Communications* **2019**, *236*, 72–85.
- (41) Abels, H.; Garcke, H.; Grün, G. Thermodynamically consistent, frame indifferent diffuse

- interface models for incompressible two-phase flows with different densities. *Mathematical Models and Methods in Applied Sciences* **2012**, *22*, 1150013.
- (42) Qian, T.; Wang, X. P.; Sheng, P. A variational approach to moving contact line hydrodynamics. *Journal of Fluid Mechanics* **2006**, *564*, 333–360.
- (43) Grün, G.; Guillén-González, F.; Metzger, S. On Fully Decoupled, Convergent Schemes for Diffuse Interface Models for Two-Phase Flow with General Mass Densities. *Communications in Computational Physics* **2016**, *19*, 1473–1502.
- (44) Bonart, H.; Kahle, C.; Repke, J. U. Comparison of energy stable simulation of moving contact line problems using a thermodynamically consistent Cahn–Hilliard Navier–Stokes model. *Journal of Computational Physics* **2019**, *399*, 108959.
- (45) Xu, X.; Di, Y.; Yu, H. Sharp-interface limits of a phase-field model with a generalized Navier slip boundary condition for moving contact lines. *Journal of Fluid Mechanics* **2018**, *849*, 805–833.
- (46) Ding, H.; Speltz, P. D. Onset of motion of a three-dimensional droplet on a wall in shear flow at moderate Reynolds numbers. *Journal of Fluid Mechanics* **2008**, *599*, 341–362.
- (47) Aland, S.; Voigt, A. Benchmark computations of diffuse interface models for two-dimensional bubble dynamics. *International Journal for Numerical Methods in Fluids* **2012**, *69*, 747–761.
- (48) Bonart, H.; Jung, J.; Kahle, C.; Repke, J. U. Influence of Liquid Density and Surface Tension on the Pinning of Sliding Droplets on a Triangular Microstructure. *Chemical Engineering and Technology* **2019**, *42*, 1381–1387.
- (49) Bonart, H.; Repke, J. U. Direct numerical simulations of liquids on microstructured surfaces: Analysing the fluid dynamics on packing. *Chemical Engineering Transactions* **2018**, *69*, 61–66.

- (50) Aland, S.; Boden, S.; Hahn, A.; Klingbeil, F.; Weismann, M.; Weller, S. Quantitative comparison of Taylor flow simulations based on sharp-interface and diffuse-interface models. *International Journal for Numerical Methods in Fluids* **2013**, *73*, 344–361.
- (51) Jacqmin, D. Calculation of Two-Phase Navier-Stokes Flows Using Phase-Field Modeling. *Journal of Computational Physics* **1999**, *155*, 96–127.
- (52) Wächter, A.; Biegler, L. T. On the implementation of an interior-point filter line-search algorithm for large-scale nonlinear programming. *Mathematical Programming* **2006**, *106*, 25–57.
- (53) Garcke, H.; Hinze, M.; Kahle, C. Optimal control of time-discrete two-phase flow driven by a diffuse-interface model. *ESAIM - Control, Optimisation and Calculus of Variations* **2019**, *25*, 13.
- (54) Alnæs, M. S.; Blechta, J.; Hake, J.; Johansson, A.; Kehlet, B.; Logg, A.; Richardson, C.; Ring, J.; Rognes, M. E.; Wells, G. N. The FEniCS Project Version 1.5. *The FEniCS Project Version 1.5* **2015**, *3*, 9–23.
- (55) Logg, A.; Mardal, K. A.; Wells, G. In *Manual*; Logg, A., Mardal, K.-A., Wells, G., Eds.; Lecture Notes in Computational Science and Engineering; Springer Berlin Heidelberg: Berlin, Heidelberg, 2012; Vol. 84; p 718.
- (56) Balay, S. et al. PETSc web page. 2018; <http://www.mcs.anl.gov/petsc>.
- (57) Balay, S. et al. *PETSc Users Manual*; 2018.
- (58) Balay, S.; Gropp, W. D.; McInnes, L. C.; Smith, B. F. Efficient Management of Parallelism in Object-Oriented Numerical Software Libraries. *Modern Software Tools for Scientific Computing*. 1997; pp 163–202.
- (59) De Ruiter, R.; Pit, A. M.; De Oliveira, V. M.; Duits, M. H.; Van Den Ende, D.;

Mugele, F. Electrostatic potential wells for on-demand drop manipulation in microchannels. *Lab on a Chip* **2014**, *14*, 883–891.

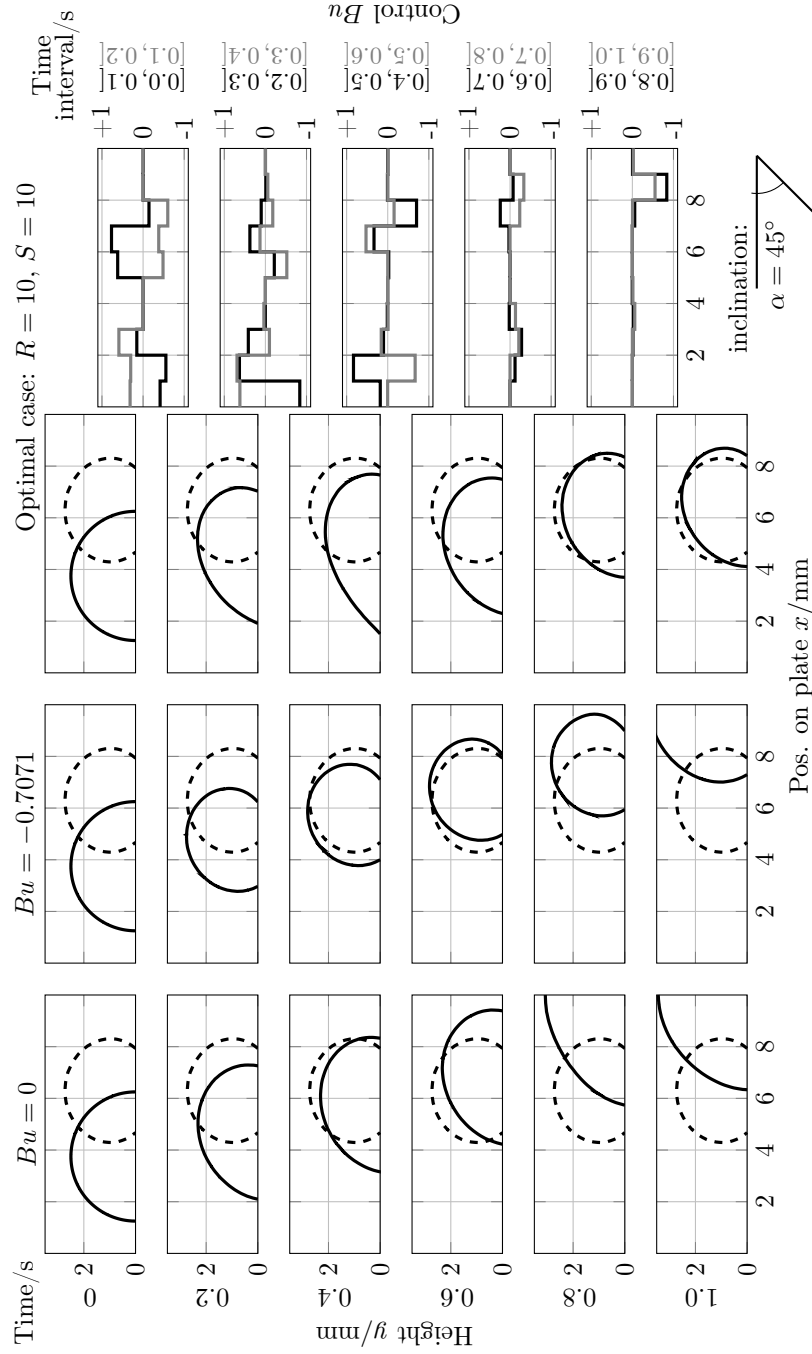


Figure 9: Development of the sliding and pinned droplets over time on a plate with an inclination to the horizontal of $\alpha = 45^\circ$: no control action with $Bu = 0$ (first column), constant control action with $Bu = -0.7071$ (second column) and optimal control action for $R = 10$ and $S = 10$ (third column). In the fourth column the optimal control action is displayed for the time intervals. The desired shape and position of the droplet φ_d is included as the dashed line.